



HAL
open science

Developing biobased and degradable polyazomethines from hemin

Ping-Jui Yu, Wei-Cheng Chen, Chih-Chien Hung, Ya-Shuan Wu, Yan-Cheng
Lin, Redouane Borsali, Wen-Chang Chen

► **To cite this version:**

Ping-Jui Yu, Wei-Cheng Chen, Chih-Chien Hung, Ya-Shuan Wu, Yan-Cheng Lin, et al.. Developing biobased and degradable polyazomethines from hemin. *Materials Today Sustainability*, 2024, 26, pp.100759. 10.1016/j.mtsust.2024.100759 . hal-04776801

HAL Id: hal-04776801

<https://hal.science/hal-04776801v1>

Submitted on 20 Nov 2024

HAL is a multi-disciplinary open access archive for the deposit and dissemination of scientific research documents, whether they are published or not. The documents may come from teaching and research institutions in France or abroad, or from public or private research centers.

L'archive ouverte pluridisciplinaire **HAL**, est destinée au dépôt et à la diffusion de documents scientifiques de niveau recherche, publiés ou non, émanant des établissements d'enseignement et de recherche français ou étrangers, des laboratoires publics ou privés.

Developing Biobased and Degradable Polyazomethines from Hemin

Ping-Jui Yu,^{a,b} Wei-Cheng Chen,^a Chih-Chien Hung,^{a,c} Ya-Shuan Wu,^a

Yan-Cheng Lin,^{c,d} Redouane Borsali,^{b,*} and Wen-Chang Chen^{a,c,*}*

^a Department of Chemical Engineering, National Taiwan University, Taipei 10617, Taiwan.

^b Centre de Recherches sur les Macromolécules Végétales (CERMAV), affiliated with Grenoble Alpes University, Institut Carnot PolyNat, BP53, 38041 Grenoble Cedex 9, France

^c Advanced Research Center for Green Materials Science and Technology, National Taiwan University, Taipei 10617, Taiwan.

^d Department of Chemical Engineering, National Cheng Kung University, Tainan 70101, Taiwan.

*Corresponding author. E-mail: ycl@gs.ncku.edu.tw (Y.-C. L.); borsali@cermav.cnrs.fr (R. B.); chenwc@ntu.edu.tw (W.-C. C.)

KEYWORDS: polyimine; phototransistors; nonvolatile memory; hemin; protoporphyrin IX

ABSTRACT

The development of biobased polymers is emerging as a critical issue for researchers in this era, especially for conjugated or semiconducting polymers, due to the lack of natural conjugated building blocks. In addition, it is of urgent importance to develop degradable polymers to diminish the increasing amount of plastic waste. Therefore, we aim to utilize hemin-based materials as a building block to develop semi-conjugated, degradable, and biobased polymers in this study. Accordingly, hemin derived from bovine is modified to remove the ferric ion and functionalize with amine or aldehyde groups. The aldehyde-functionalized protoporphyrin is copolymerized with *p*-phenylenediamine, 2,7-fluorenediamine, and amine-functionalized protoporphyrin to form a series of polyazomethines of **PDA**, **FDA**, and **PPIX**. The semi-conjugated polyazomethines exhibit varied electrostatic potential distributions and frontier energy levels based on their compositions; in addition, all the polyazomethines present high biomass contents spanning the range of 60-80%. Notably, **PPIX** can be rapidly depolymerized by acid hydrolysis with 0.01 M of HCl within several hours, guaranteed by the evolutions of optical absorption and size-exclusion chromatography, which show that the polyazomethines degrade to monomers to short-chain oligomers. In the aspect of the optoelectronic device application, the semi-conjugated characteristics of the hemin-based polyazomethines give rise to their high performance as a photoresponsive polymer electret in photonic transistor memory. By fine-tuning the molecular structure and energy levels, the developed polyazomethine of **FDA** achieves decent data discernibility and long-termed cyclic operation as a component of memory electronics, thereby rendering green electronics exceptionally economical and environmentally feasible.

INTRODUCTION

With burgeoning demand for energy-saving and exploration of fossil fuels, the awareness of high added-value and eco-friendly materials has been attracted to numerous studies. However, maintaining materials' performance while using biobased substituents remains a formidable challenge for social humanity. With this regard to the development of optoelectronic devices, it is of utmost importance to develop semi-conjugated and biobased materials to diminish the electronic wastes and modulate their performance in applications of nonvolatile memory, anti-counterfeiting and data encryption devices, display, and bioimaging technology, simultaneously. For instance, with the fast and remote stimuli of light, the advantages of digital photoprogramming include low energy consumption, ultrafast speed writing speed, and high data capacity. Recent studies have focused on organic or organic/inorganic hybrid optoelectronic devices, including phototransistor¹⁻³, photosynaptic⁴⁻⁷, and photoswitchable displays^{8,9}. In particular, the photonic transistor memory has been extensively investigated and regarded as a pioneer for multilevel data storage. With the orthogonal operation of the light programming and electric stimuli, the digits are stored in chargeable electrets materials. Then, the storage information is read by other stimuli and recorded in the distinguishable memory states. However, most conventional photoresponsive materials are toxic to the environment and harmful to humans, restricting their processability to produce; mainly, the photoactive perovskite nanoparticles or quantum dots, which set off a wave of widely-utilizing light-harvesting materials but make less contribution to mitigate their impact on the environments. To address these concerns, using green materials is regarded as an urgent requirement for researchers in this era.

As a seemingly old but still trending natural dye, hemin was discovered by H. Fischer and awarded Nobel Prize in 1930. With the incomparable advantages of multifunctionality and structural tunability for biomimetic catalysts or biosensors¹⁰⁻¹³; environmental stability, chemostability (alkaline and acidic), and photostability under ambient atmosphere due to its macrocyclic structure¹⁴⁻¹⁶; cost-effectiveness and high affordability due to the increased availability from mammals especially from biological residues of bovines; UV and visible light absorption and light sensitivity crediting from the

protoporphyrin core, thereby emitting green to red light spanning the range of 590 to 660 nm after excitation at 400 nm light; redox electroactivity associated with its macrocyclic structure complex¹⁷⁻¹⁹. Therefore, hemin is considered a promising green and conjugated molecule from nature.

Although the application of biobased materials burgeoning emerges, electronic waste is still another issue required to tackle in the high-tech era. Numerous shreds of evidence developed degradable materials on charge storage and optoelectronic devices inspired by renewable and reusable materials. However, only a few pieces of research are dedicated to harnessing biobased materials to optoelectronic devices concerning degradability and sustainability while warranting their device performance comparable with their petroleum-based counterparts²⁰. With regard to the degradable materials in photomemory, Chen *et al.* utilized isosorbide as a biobased building block and polymerized with fluorene to form a series of polyazomethines. As expected herein, imine linkages are demonstrated to enhance the charge-trapping characteristics of the phototransistor memory. In addition, the polymers could be degraded with trifluoroacetic acid hydrolysis after a week. However, the non-conjugated isosorbide must be copolymerized with another petroleum-derived conjugated building block for achieving visible-light sensitivity, thereby confining the biomass content of these polyazomethines to approximately 20%. With regard to the stretchable field-effect transistors (FETs), Tran *et al.* developed a series of diketopyrrolopyrrole-based conjugated polyazomethines to show decent degradability and comparable mobility with the conventional diketopyrrolopyrrole-based conjugated polymers. However, the building blocks utilized are all from petroleum sources, and they will be released after depolymerization which will be toxic to biologies, thereby confining their environmental compatibility and sustainability^{21, 22}. Indeed, they took advantage of an imine group as the degradable function group via fluoric acid treatment, confirmed by UV-vis absorption and IR spectrum after degraded. On the other hand, it is cognizant that the degradable functional group can be breakdown into small moieties through acid treatment^{23, 24}. Zhao *et al.* even verified the recyclable and malleable imine bonds in thermoset polymers, contributing to the galloping developments of environmental-friendly electronics in modern communication²⁵.

Therefore, we aim to utilize hemin-based materials as a building block to develop semi-conjugated, degradable, and biobased polymers. In this study, hemin derived from bovine is modified to remove the ferric ion and functionalize with amine or aldehyde groups. The aldehyde-functionalized protoporphyrin was copolymerized with *p*-phenylenediamine, 9*H*-fluorene-2,7-diamine, and amine-functionalized protoporphyrin to form a series of polyazomethines of **PDA**, **FDA**, and **PPIX**, respectively. Through the formation of imine linkages, all polyazomethines studied showed sufficient degradability within several hours along with high biomass contents over 60 %. The semi-conjugated polyazomethines exhibited different electrostatic potential distributions and frontier energy levels based on their compositions. Concerning the tunable electronic and optical properties, the polyazomethines were designed and applied in phototransistor memory. Accordingly, the biobased polyazomethines were utilized as a photoresponsive electret and thermally deposited with copper phthalocyanine (CuPC) as a high-performance channel^{26,27}, which potentially originated from natural phthalimide²⁸⁻³⁰. The phototransistor memory were systematically investigated on their carrier mobility, memory parameters, and long-term/endurance stability. This work utilizes hemin-derivatives featured as high biomass content, low cost, environmentally friendly, and degradable alternative for the design of green and semi-conjugated polymers.

EXPERIMENTAL SECTION

Materials. All the reagents and solvents were commercially available and were directly utilized without further purification, except for iron(II) sulfate heptahydrate ($\text{FeSO}_4 \cdot 7\text{H}_2\text{O}$) was dehydrated under a heating vacuum at 140 °C for three days prior to use. Hemin (>95.0%), *p*-nitrobenzophenol (>99.5%), *N,N*-diisopropylethylamine (DIPEA, >99.0%), 1,4-phenylenediamine (>98%), and 2,7-diaminofluorene (>98.0%) were purchased from TCI (Japan). Acetic anhydride ($(\text{AcO}_2)_2\text{O}$, >99.0%), iron(II) sulfate heptahydrate ($\text{FeSO}_4 \cdot 7\text{H}_2\text{O}$), hydrochloric acid (HCl, 37.0%), *p*-hydroxybenzaldehyde (>99.0%), *N*-(3-dimethylaminopropyl)-*N'*-ethylcarbodiimide hydrochloride (EDC-HCl, powder), 4-(dimethylamino)pyridine (DMAP, $\geq 99.0\%$), hydrazine (H_2NNH_2 , 35 wt% in H_2O), palladium on

carbon (Pd/C), *p*-toluenesulfonic acid monohydrate (PTSA \geq 98.5%), calcium chloride (CaCl₂, granular, \geq 93.0%), *N,N*-dimethylformamide (DMF, 99.8%), and *N,N*-dimethylacetamide (DMAc, 99.8%) were obtained from Sigma Aldrich (USA). Copper(II) phthalocyanine (CuPC, >99%) was purchased from Lumtec Corp. (Taiwan).

Characterization. ¹H and ¹³C NMR spectra were obtained using a Bruker DPX400 MHz spectrometer at the resonant frequencies at 400 MHz with deuterated dimethylsulfoxide (DMSO-*d*₆) as a solvent for monomers and polyazomethines. The weight average molecular weight of the polymers synthesized were recorded by a size exclusion chromatograph (SEC) in Enshine SUPER CO-150 equipped a UV-visible detector and two polystyrene gel columns (Stryagel HR2 and styragel 4) with DMF as an eluent at a flow rate of 1.0 mL min⁻¹ calibrated by standard polystyrene. The elemental compositions of the monomers were investigated by using an elementary analyzer (EA), Elementar vario EL cube. The operating condition was performed with the combustion tube at 1150 °C and the reduction tube at 800 °C assisted with the oxygen flux rate at 2.2 kg cm⁻² and of the helium flux rate at 1.2 kg cm⁻². Fourier-transform infrared spectroscopy (FT-IR, Spectrum Two FT-IR L160000F, PekinElmer) visualized the functional groups in a range of wavenumber from 500 to 4000 cm⁻¹. The decomposition temperature at 5 wt% weight loss ($T_d^{5\%}$) was evaluated by thermogravimetric analysis (TGA, TA instrument TGA 25) at a heating 10 °C min⁻¹ until 700 °C. The phase transition temperature (T_g) was obtained from differential scanning calorimetry (DSC, TA instrument DSC 25) with a ramping rate of 10 °C min⁻¹ under nitrogen atmosphere repeatedly for a period of two consecutive cycles. The ultraviolet–visible (UV–vis) absorption spectra were recorded on a Hitachi U-4100 spectrophotometer with the scanning ranging from 800 to 250 nm. The corresponding band gap (E_g^{opt}) of the polyazomehtines studied were calculated from the onset of UV-vis spectra as the following formula: E_g^{opt} (eV)= 1240/ λ_{onset} (nm). The photoluminescence (PL) emissions spectra were measured by a Horiba Fluorolog-3 spectrometer system scanning from 400 to 850 nm. The electrochemical properties of the polyazomethines studied were measured via cyclic voltammetry (CV) on the potential window

from 0 to 2.0 V at a scan rate of 100 mV s⁻¹ under a nitrogen atmosphere by using a CHI 6273E electrochemical analyzer with the three-electrode assembly with 0.1 M tetrabutylammonium perchlorate (TBAP) in anhydrous acetonitrile as an electrolyte. The three-electrode cell consisted with an indium tin oxide (ITO) substrate spin-coated with the polymers studied, a platinum wire, and an Ag/AgNO₃ reference for the working electrode, auxiliary electrode, and reference electrode, respectively. The morphological topography of the polyazomethines studied were evaluated using a Bruker Innova Atomic Force Microscope (AFM) operated under tapping mode at a resonance frequency of 330 kHz.

Fabrication and Characterization of the Phototransistor Memory Device. The p-type field-effect transistor (FET) and phototransistor memory devices were fabricated based on a 100 nm SiO₂/n-doped Si substrate with the bottom-gate/top-contact (BG/TC) architecture. The photoresponsive electret layer was prepared by spin-coating the polyazomethine solution with a concentration of 5 mg ml⁻¹ at a spin rate of 1500 rpm for 60 s, following by 3000 rpm for 10 s, and the polymer film was annealed at 140 °C for 30 min. After cooling to room temperature, the CuPC semiconducting channel was deposited under vacuum (10⁻⁷ torr) at a deposition rate of ca. 0.2 Å s⁻¹ to afford a thickness of 50 nm. Finally, to define the top-contact channel electrodes, a 45-nm-thick film of gold was thermally deposited at a rate of 0.5 Å s⁻¹ via a shadow mask with a channel width (W) and length (L) of 50 and 1000 μm, respectively. The phototransistor memory was characterized by using a Keithly 4200-SCS with a Remote PreAmp (4200-PA) in a nitrogen-filled glove box. The corresponding parameters of typical FETs were estimated in the saturation regime as the followed equation: $I_D = (W \times C_s \times \mu_{th}) \times (V_g - V_{th})^2 / 2L$, where W and L are the Au channel width and length. I_D is the drain current, C_s is the capacitance of the SiO₂ dielectric (31.5 nF cm⁻²), and V_g is the gate voltage. The typical FET values of hole mobility (μ_{th}) and threshold voltage (V_{th}) were extracted from the saturation regime of the transfer curve accordingly. For characterization of phototransistor memory, the light programming was conducted with 450-nm light at an intensity of 0.95 mW cm⁻².

RESULTS AND DISCUSSIONS

Syntheses and Characterizations of the Hemin-based Polyazomethines. In this study, the route of monomer synthesis is displayed in **Scheme 1a**. The synthesis proceeded from commercially available hemin in three steps: (i) removal of ferric ion, (ii) esterification on acid groups to functionalize amine or aldehyde groups, (iii) and then imino polymerization for polyazomethines. Initially, hemin was treated with $\text{FeSO}_4/\text{HCl}/(\text{AcO}_2)\text{O}$ at 100 °C for an hour to remove the central chelated ferric ion. Steglich esterification was subsequently underwent with the addition of either *p*-nitrobenzophenol or *p*-hydroxybenzaldehyde, leading to the aldehyde-terminated protoporphyrin, **HCHO**, or the nitro-terminated protoporphyrin, **HNO2**, respectively. The reduction of the nitro group of **HNO2** occurred subsequently under hydrazine and Pd/C catalyst to acquire the amine-terminated protoporphyrin, **HNH2**. For the polymerization, **HCHO** was copolymerized with *p*-phenylenediamine, 2,7-fluorenediamine, and **HNH2** to form a series of polyazomethines of **PDA**, **FDA**, and **PPIX** via microwave-assisted reactor at 180 °C, as shown in **Scheme 1b**. The synthetic procedures are detailed in the Supporting Information, and the chemical structures of the monomers and polymers were characterized and are presented by ^1H and ^{13}C NMR spectra and elementary analyses in **Figures S1-S7** (Supporting Information). All the elementary compositions and estimated chemical shifts of the precursors and as-obtained polyazomethines agreed with good relevance to their predicted values. Through the formation of imine linkages, all polyazomethines studied showed high biomass contents spanning the range of 60-80%. In addition, they also have excellent solubility in high-polarity solvents, such as DMF, DMSO, and DMAc. The molecular weight of the three resulting products was investigated by using DMF-based SEC with 280-nm UV light detection, as shown in **Figure S8** (Supporting Information), and the derived molecular weight information are summarized in **Table 1**. As can be seen, all the hemin-based polyazomethines, **PDA**, **FDA**, and **PPIX**, demonstrated the number-averaged molecular weights (M_n) and polydispersity index (D) ranging from 8100 to 10000 g

mol⁻¹ and 2.77 to 4.30, respectively. The results indicated the successful polymerization of biobased polyazomethines with comparable molecular weights.

After the synthesis of the polyazomethines was established, their thermal properties were next investigated. The corresponding thermal parameters are summarized in **Table 1**. As presented in **Figure S9a** (Supporting Information), the TGA profiles of the polyazomethines studied indicated their $T_d^{5\%}$ are in the range of 180-260 °C. **Figure S9b** (Supporting Information) displays the DSC profiles of these polymers, **FDA** and **PPIX** exhibited glass transition temperature (T_g) at approximately 30 and 60 °C, respectively. In addition, **PPIX** also presented a melting point at approximately 130 °C. As obtained, both **PPIX** and **FDA** provided comparable $T_d^{5\%}$ and well-defined T_g , and they also remained high char residual yields after heating up; in contrast, **PDA** exhibited the lowest $T_d^{5\%}$ among the three polymers studied and even no T_g .

Molecular Simulation of the Polyazomethines Studied. The optimized configurations of the polyazomethines studied were simulated by using density functional theory (DFT). The B3LYP method with 6-31G level basis was applied for ground-state molecular geometry simulation. Two repeating units were used to calculate the polymers studied to achieve the optimized configuration and evaluated frontier energy levels. **Figure 1a** displays the electrostatic potential mapping of the polymers studied. As can be seen, **PDA** and **PPIX** possessed donor-donor structures with electrostatic potential concentrated locally. In contrast, the donor-acceptor structure of **FDA** formed by fluorene and protoporphyrin exhibited spatially allocated electrostatic potential distribution, which is beneficial for intermolecular charge transfer interaction. Next, the DFT calculation is applied to gain insight into the frontier energy levels of the highest occupied/lowest unoccupied molecular orbitals (HOMO/LUMO). The frontier energy levels HOMO-1, HOMO, LUMO, and LUMO+1 with their electron distribution in DFT simulated microstructure are schematically illustrated as in **Figure S10** (Supporting Information). The LUMO+1, LUMO, HOMO, and HOMO-1 levels are (-2.25, -2.28, -5.11, -5.13) eV, (-2.29, -2.33, -5.07, -5.10) eV, and (-2.21, -2.24, -5.03, -5.06) eV for **PDA**, **FDA**, and **PPIX**,

respectively. The simulated bandgaps are 2.83, 2.74, and 2.79 eV for **PDA**, **FDA**, and **PPIX**, respectively. As can be seen, the donor-acceptor structure of **FDA** effectively narrows the energy bandgap.

Optical and Electrochemical Properties of the Biobased Polyazomethines. The optical property was investigated next by using UV-vis absorption, photoluminescence (PL) emission spectroscopies, and cyclic voltammetry (CV) experiments. The relative parameters including maximal absorption wavelength (λ_{\max}), onset wavelength (λ_{onset}) of the UV-vis absorption, and the extracted optical energy gap (E_g^{opt}) are summarized in **Table 1**. **Figures 1b** and **S11a** (Supporting Information) display UV-vis absorption spectra of the polymers in film or solution states. As can be seen, all hemin-based polyazomethines showed λ_{\max} at 400 nm in the thin film state and λ_{\max} at 410 nm in the DMF solution. All the hemin-based derivatives exhibited the Soret band referred to $\pi \rightarrow \pi^*$ transition, which consisted of both HOMO-1 \rightarrow LUMO+1 and HOMO \rightarrow LUMO+1 excitation. In the range of 480 to 650 nm, the free-based porphyrin typically featured as the Q band splitting from the combination of HOMO-1 \rightarrow LUMO or denoted as Q_x , and HOMO \rightarrow LUMO or denoted as Q_y , excitation, while x and y defined as the perpendicular orientation of the electronic transition dipole moments. Two shorter-wavelength bands at 505 and 530 nm indicated the electric transition dipole moment on the x-axis as a pure electron excitation with molecular vibration and no molecular vibrations, which are called $Q_{x,1}$ and $Q_{x,0}$, respectively. In contrast, another two longer-wavelength bands at 570 and 630 nm, which are the electric transition dipole moment on the y-axis as a pure electron excitation with molecular vibration and no molecular vibrations, are termed $Q_{y,1}$ and $Q_{y,0}$, respectively³². The protoporphyrin without a ferric ion presents two relatively weaker bands separated according to the two symmetric peripheral amine groups. However, the maxima absorption peak features a blue shift from the solution to the solid state, presumably due to diminished dimensional spacing. Moreover, the λ_{onset} of **PDA**, **FDA**, and **PPIX** is at 458, 459, and 454 nm, respectively, and the corresponding E_g^{opt} is 2.71, 2.70, and 2.73 eV, respectively, which are in good relevance with DFT calculated values. The λ_{\max} of **PDA**,

FDA, and **PPIX** is at 409, 411, and 410 nm, respectively. The slightly red shift of **FDA** and **PPIX** is attributed to their constraint of the adjacent moiety, fluorene and protoporphyrin, indicating both lower energy required to procedure electron transition³¹.

Figures 1c and **S11b** (Supporting Information) are PL emission spectra with the excitation wavelengths at 400 and 410 nm as the maximal absorption wavelengths in the solid and solution states, respectively. As presented in **Figure 1c**, all polyazomethines exhibited PL emission maxima peaks at 560 nm in the solid with a weak band at around 640 to 700 nm. In contrast, the emission profiles of **PPIX** shows the PL emission maxima peak located at 625 nm in the DMF solution state with a broad shoulder until 720 nm, indicating its different molecular packing structure. After investigating the optical properties, CV provides the redox potentials and electrochemical properties of the polymers studied, as displayed in **Figure S12** (Supporting Information). Combining the CV profile and UV-vis absorption spectrum, the frontier molecular orbitals levels were extracted and are summarized in **Figure 1d** and **Table 1**. The HOMO/LUMO levels of **PDA**, **FDA**, and **PPIX** are -4.73/-2.02 eV, -5.05/-2.35 eV, and -4.69/-1.96 eV, respectively. The donor-acceptor structure of **FDA** effectively lowers the energy levels owing to the charge transfer interaction from protoporphyrin to the electron-withdrawing fluorene group. In contrast, donor-donor structures in **PDA** and **PPIX** features an additional electron-donating property to elevate the energy levels. These results are in good accordance with those predicted from the optimized molecular structures by using DFT calculations.

Depolymerization Studies of the Biobased Polyazomethines. In order to investigate the degradability of the polymers studied, **PPIX** with a high biomass content was applied to demonstrate its sustainability, and the depolymerization process was tracked by using UV-vis absorption spectra, FT-IR spectra, and SEC profile, as described in **Figure 2**. Due to the cleavable imine bond under acid hydrolysis, polyazomethines was depolymerized by using 0.01 M HCl in DMF solution. By observing the UV-vis absorption profiles, the process of depolymerization was tracked. **Figure 2b** provides the UV-vis absorption spectra to describe the dynamic degradation at different time intervals until 5 days.

The corresponding λ_{\max} traces migrated from 410 nm toward a lower wavelength of 390 nm within the first hour, and the polymer signal decreased rapidly in the following hours. Finally, the **PPIX** sufficiently depolymerized after 7 hrs, and the optical absorption profiles remained similar along 5 days. As can be seen in **Figure 2c**, the FT-IR spectra indicated that the imine groups degraded to the aldehyde and amine groups after acid hydrolysis. After the addition of the HCl, the signal of the imine group (C=N stretching at 1595 cm^{-1}) in **PPIX** diminished, and the appearance of aldehyde (C=O stretching at 1631 cm^{-1} , C-H stretching at 2783 cm^{-1} , and C-H bending at 1449 cm^{-1}) and amine group (NH_2 at 3375 cm^{-1}) ensured the depolymerization. In addition, the depolymerization-induced molecular weight variation was recorded in SEC trace with DMF as an eluent, as presented in **Figure 2d**. As can be seen, there is no detectable signal spanning the range of 10 to 25 mins, indicating the sufficient depolymerization of **PPIX**. **PPIX** not only secures a high biomass content but also degrades into smaller biobased molecules, which is beneficial for sustainability and viability of biobased electronics.

Phototransistor Memory Application of the Polyazomethines Studied. Benefiting from the cost-effectiveness, high biomass content, and chemical stability, the polyazomethines studied were used as photoresponsive electrets in the BG/TC FET device. **Figure 3a** displays the architecture and chemical structures of the constituent materials in the phototransistor memory. CuPC was applied as a semiconducting channel owing to the molecular similarity with the hemin-based polyazomethines³³. As depicted in **Figure S13** (Supporting Information), the transfer curve of regular FET device comprising CuPC ensures the typical p-channel behavior and the classic p-type accumulation with the corresponding hole mobility (μ_h) of $2.3 \times 10^{-3}\text{ cm}^2\text{ V}^{-1}\text{ s}^{-1}$, threshold voltage (V_{th}) of -0.21 V , and current contrast of 6.8×10^3 . After the incorporation of polymer electret as described in the Experimental Section, the characterization of memory devices was performed under a dark environment to avoid disruption from light. The gate voltage (V_G) was swept from 20 to -60 V at a fixed drain voltage (V_D) of -60 V . As **Figures 3b-d** depicted, the memory devices with a polyazomethine electret presented decreased μ_h between 1×10^{-5} to $6 \times 10^{-5}\text{ cm}^2\text{ V}^{-1}\text{ s}^{-1}$, $I_{\text{on/off}}$ values between 1.0×10^2 to 1.9×10^3 , and

increased V_{th} values of 0 to -9.5 V. The relatively low μ_h is due to the intrinsic hole-trapping property of the polyazomethine electret, resulting in the hole carriers being trapped in the chargeable electrets. Among them, **PDA** and **FDA** exhibited higher μ_h of 5.0×10^{-5} and 5.9×10^{-5} $\text{cm}^2 \text{V}^{-1} \text{s}^{-1}$, which is ascribed to the lower-lying energy levels credited from the donor-acceptor structure. In contrast, **PPIX** presented the lowest hole-transport capability, which can also be attributed to the strong aggregation of **PPIX**, as can be seen in the AFM morphology in **Figure S14** (Supporting Information). The AFM surface roughness (R_q) of **PDA**, **FDA**, and **PPIX** are 1.31, 6.68, and 10.3 nm, respectively. The R_q of **PDA** acquired smoother surfaces than **FDA**, indicating better compatibility with the semiconducting layer atop. In comparison, **PPIX** presented the highest R_q , straightly affecting the above semiconducting layer and charge transport. With regard to the surface morphology of CuPC channel, **Figure S16** (Supporting Information) displays their AFM images on different polyazomethine electrets. The resulting R_q of **PDA**, **FDA**, and **PPIX** are 5.56, 5.97, and 18.3 nm, respectively, while the R_q of pristine CuPC thin film is 2.79 nm. The R_q of CuPC on **FDA** is comparable to **PDA**, which renders the flattened and crystalline surface to facilitate charge transport and reduce the interfacial defects. In contrast, the strong aggregation of **PPIX** contributed from the intrinsic restriction of the bond torsion. The lack of movable adjacent moiety leads poor compatibility and a substantial defect-rich interface between the interfacial surfaces.

With memory programming in **Figure 3b-d**, the transfer curves were shifted to negative regime in response to a negative impetus assisted by V_G of -60 V. Next, the light illumination (450 nm; 0.95 mW cm^{-2} ; 5 s) was applied to shifted back the transfer curves to their initial state. The memory window (ΔV_{th}) is defined by the V_{th} difference between the “ON” state after electrical writing and the “OFF” state after photoerasing. The memory ratio ($I_{on/off}$) is defined at $V_G = -20$ V between these two memory states. The relevant memory device parameters are summarized in **Table 1**. As can be seen in **Figure 3c**, **FDA** possesses a good ΔV_{th} of 31.4 V and the highest $I_{on/off}$ of 1.9×10^3 A among the polyazomethines studied, implying the best performance of the phototransistor owing to the donor-acceptor molecular structure associated with favorable frontier energy levels alignment with CuPC,

thereby promoting the charge separation and transportation compared with other systems. The transient photocurrent measurements of the memory devices are shown in **Figure S16** (Supporting Information). All the device currents boosted from 10^{-12} A to over 10^{-9} A with 450-nm light illumination at $V_D = -60$ V. The results describe the memory devices comprising biobased polyazomethines exhibited rapid photoresponse and well-defined memory states.

Long-term storage capability has been cognizant as an important index for memory devices. As **Figure 3e** demonstrated, the polyazomethines-based phototransistor memory recorded the corresponding I_{SD} after the blue light illumination for 1 s (low-resistance state) or gate impetus of $V_g = -60$ V for 5 s (high-resistance state) over 8,000 s. Among them, **FDA** exhibited the most stable and the highest $I_{on/off}$ of 10^4 , which is 2-3 orders higher than other counterparts. In addition, write-reading-erasing-reading (WRER) test also implies the repeatedly switching ability as another crucial index for memory devices. As **Figure 3f** and **Figure S17** (Supporting Information) illustrated, the bistable switchability were achieved under electrical writing with $V_g = -60$ V for 1 s; photoerasing (450 nm; 0.95 mW cm^{-1} ; 10 s) at $V_d = -20$ V for 10 s; reading at $V_d = -20$ V for 10 s without gate impetus for 30 consecutive cycles. The corresponding I_{SD} was recorded along with time. Notably, **FDA** presented the bistable low-resistance state at $\approx 10^{-9}$ A and high-resistance state at $\approx 10^{-12}$ A, exhibiting the highest $I_{on/off}$ of 10^3 among the systems studied. The result confirms the high performance of superior long-term stability and data discernibility achieved by using hemin-based polyazomethine as an electret in phototransistor memory.

By virtue of the aforementioned characteristics, including optical, electronic, and morphological properties, **Figure 4** illustrates a plausible mechanism to decipher the structure-performance relationship of polyazomethines in phototransistor memory. In the initial state, the hole carriers migrated at the interfaces between the memory layer and active layer. After applying a negative gate impetus of -60 V, hole carriers were injected into the electret to afford an “ON” state. Through sweeping the transfer curves, the device was switched to a high resistance with largely negative threshold voltage. After applying light illumination, excitons generated in the electret were dissociated

and the photoinduced electrons were recombined with the trapped holes; while the photoinduced holes tunneled into the channel in response to the negative drain voltage. Therefore, the device was switched to an “OFF” state. Through sweeping the transfer curves, the device was switched to a low resistance with a threshold voltage close to zero. Owing to the red-shifted optical absorption of CuPC spanning the range of 600 to 700 nm, the photoresponse contributed from the semiconducting channel is regarded to be negligible compared with the polyazomethine electrets with optical absorption spanning the range of 350 to 450 nm. Therefore, the photoerasing behavior is chiefly contributed by the photogenerated exciton in the electret after blue-light irradiation^{34,35}. It has been proved that the excitons dissociated separately at the interfaces according to the electrostatic potential distribution of the molecular structures²². The electrons promptly migrated to the interface to eliminate the injected hole from electrical programming; meanwhile, the drain currents neutralized the remaining counterparts from the trapping sites in chargeable electret, indicating the stored charges were eliminated. Then the resultant device is recovered with photoerasing programming to the initial state, according to the transfer curves shift forth and back. Notably, the improved device performance is attributed to the optimized electrostatic potential distribution, fine-tuned energy level alignment with the CuPC channel, donor-acceptor structure formed by fluorene and protoporphyrin. By fine-tuning the molecular structure and energy levels, the developed polyazomethine of **FDA** achieves decent data discernibility and long-termed cyclic operation for nonvolatile memory application while exhibiting the sustainability and viability for green electronics.

CONCLUSION

On the basis of natural hemin, the biobased and degradable polyazomethines were engineered with diverse moieties of benzene, fluorene, and protoporphyrin for **PDA**, **FDA**, and **PPIX**, respectively. Through the formation of imine linkages, all polyazomethines studied showed sufficient degradability within several hours along with high biomass contents over 60 %. **PPIX** demonstrated a high biomass content of about 80 %, which also simultaneously provided rapid degradability within several hours

warranted by UV-vis absorption spectra, FT-IR spectra, and SEC traces after acid hydrolysis with 0.01 M HCl. The degradation results disclosed the fast diminishment of the imine groups in the polyazomethines, indicating their depolymerization. Concerning the tunable electronic and optical properties, the polyazomethines were designed and applied in phototransistor memory. It is cognizant that rapid photoresponsivity, bistable discernibility, and long-term bistable digitals were exceeded by the phototransistor memory comprising hemin-based polyazomethines. Among them, the best performance in photonics and electronics was specifically carried out by **FDA**, and it is attributed to (i) the optimized electrostatic potential distribution; (ii) fine-tuned energy level alignment with the CuPC channel; (iii) donor-acceptor structure formed by fluorene and protoporphyrin. Therefore, of the photonic transistor memory, **FDA** outperforms with memory performance of $I_{\text{on/off}} = 1.85 \times 10^3$ A and $\Delta V_{\text{th}} = 31.4$ V, signifying the bistable stability for digitals storages over a long-termed operation. As an outcome, it is believed that the biobased polyazomethines exhibited excellent sustainability and viability for green electronics.

ASSOCIATED CONTENT

Supporting Information. The Supporting Information is available free of charge on the ACS Publications website. Synthetic procedures and NMR characterizations of the hemin-based monomers and polymers; TGA and DSC thermal histograms; electrochemical analysis by CV measurement; UV-Vis absorption and PL emission spectra of polymer solutions; AFM phase images; transfer characteristics of the transistor memory devices.

AUTHOR INFORMATION

Corresponding Author

*E-mail: ycl@gs.ncku.edu.tw (Y.-C. L)

*E-mail: borsali@cermav.cnrs.fr (R. B.)

*E-mail: chenwc@ntu.edu.tw (W.-C. C)

Notes

The authors declare no competing financial interest.

ACKNOWLEDGMENT

The authors thank the financial supports from the Featured Area Research Center Program within the framework of the Higher Education Sprout Project by the Ministry of Education (112L9006). Y.-C. L. also thanks the financial support from the National Science and Technology Council in Taiwan (NSTC 111-2222-E-006-020-MY2) and the Higher Education Sprout Project, Ministry of Education to the Headquarters of University Advancement at National Cheng Kung University (NCKU).

REFERENCES

1. Leydecker, T.; Herder, M.; Pavlica, E.; Bratina, G.; Hecht, S.; Orgiu, E.; Samorì, P., Flexible non-volatile optical memory thin-film transistor device with over 256 distinct levels based on an organic bicomponent blend. *Nature Nanotechnol.* **2016**, *11* (9), 769-775.
2. Han, T.; Wang, Z.; Shen, N.; Zhou, Z.; Hou, X.; Ding, S.; Jiang, C.; Huang, X.; Zhang, X.; Liu, L., Diffusion interface layer controlling the acceptor phase of bilayer near-infrared polymer phototransistors with ultrahigh photosensitivity. *Nature Commun.* **2022**, *13* (1), 1332.
3. Song, J.-K.; Kim, J.; Yoon, J.; Koo, J. H.; Jung, H.; Kang, K.; Sunwoo, S.-H.; Yoo, S.; Chang, H.; Jo, J.; Baek, W.; Lee, S.; Lee, M.; Kim, H. J.; Shin, M.; Yoo, Y. J.; Song, Y. M.; Hyeon, T.; Kim, D.-H.; Son, D., Stretchable colour-sensitive quantum dot nanocomposites for shape-tunable multiplexed phototransistor arrays. *Nature Nanotechnol.* **2022**, *17* (8), 849-856.
4. Pradhan, B.; Das, S.; Li, J.; Chowdhury, F.; Cherusseri, J.; Pandey, D.; Dev, D.; Krishnaprasad, A.; Barrios, E.; Towers, A.; Gesquiere, A.; Tetard, L.; Roy, T.; Thomas, J., Ultrasensitive and ultrathin phototransistors and photonic synapses using perovskite quantum dots grown from graphene lattice. *Sci. Adv.* **2020**, *6* (7), eaay5225.
5. Lee, H. R.; Lee, D.; Oh, J. H., A Hippocampus-Inspired Dual-Gated Organic Artificial Synapse for Simultaneous Sensing of a Neurotransmitter and Light. *Adv. Mater.* **2021**, *33* (17), 2100119.

6. Shi, J.; Jie, J.; Deng, W.; Luo, G.; Fang, X.; Xiao, Y.; Zhang, Y.; Zhang, X.; Zhang, X., A Fully Solution-Printed Photosynaptic Transistor Array with Ultralow Energy Consumption for Artificial-Vision Neural Networks. *Adv. Mater.* **2022**, *34* (18), 2200380.
7. Yang, W.-C.; Lin, Y.-C.; Inagaki, S.; Shimizu, H.; Ercan, E.; Hsu, L.-C.; Chueh, C.-C.; Higashihara, T.; Chen, W.-C., Low-Energy-Consumption and Electret-Free Photosynaptic Transistor Utilizing Poly(3-hexylthiophene)-Based Conjugated Block Copolymers. *Adv. Sci.* **2022**, *9* (8), 2105190.
8. Yu, M.; Zhang, P.; Krishnan, B. P.; Wang, H.; Gao, Y.; Chen, S.; Zeng, R.; Cui, J.; Chen, J., From a Molecular Toolbox to a Toolbox for Photoswitchable Fluorescent Polymeric Nanoparticles. *Adv. Funct. Mater.* **2018**, *28* (46), 1804759.
9. Zheng, Z.; Hu, H.; Zhang, Z.; Liu, B.; Li, M.; Qu, D.-H.; Tian, H.; Zhu, W.-H.; Feringa, B. L., Digital photoprogramming of liquid-crystal superstructures featuring intrinsic chiral photoswitches. *Nature Photon.* **2022**, *16* (3), 226-234.
10. Raichlin, S.; Pecht, I.; Sheves, M.; Cahen, D., Protein Electronic Conductors: Hemin–Substrate Bonding Dictates Transport Mechanism and Efficiency across Myoglobin. *Angew. Chem. Int. Ed.* **2015**, *54* (42), 12379-12383.
11. Alsharabasy, A. M.; Pandit, A.; Farràs, P., Recent Advances in the Design and Sensing Applications of Hemin/Coordination Polymer-Based Nanocomposites. *Adv. Mater.* **2021**, *33* (2), 2003883.
12. Geng, R.; Chang, R.; Zou, Q.; Shen, G.; Jiao, T.; Yan, X., Biomimetic Nanozymes Based on Coassembly of Amino Acid and Hemin for Catalytic Oxidation and Sensing of Biomolecules. *Small* **2021**, *17* (19), 2008114.
13. Gao, Y.; Wang, J.; Feng, Y.; Cao, N.; Li, H.; de Rooij, N. F.; Umar, A.; French, P. J.; Wang, Y.; Zhou, G., Carbon–Iron Electron Transport Channels in Porphyrin–Graphene Complex for ppb-Level Room Temperature NO Gas Sensing. *Small* **2022**, *18* (11), 2103259.
14. Zhao, Y.; Zhang, Y.; Liu, A.; Wei, Z.; Liu, S., Construction of Three-Dimensional Hemin-Functionalized Graphene Hydrogel with High Mechanical Stability and Adsorption Capacity for Enhancing Photodegradation of Methylene Blue. *ACS Appl. Mater. Interfaces* **2017**, *9* (4), 4006-4014.
15. Niu, X.; Liu, Y.; Li, X.; Wang, W.; Yuan, Z., NIR Light-Driven Bi₂Se₃-Based Nanoreactor with “Three in One” Hemin-Assisted Cascade Catalysis for Synergetic Cancer Therapy. *Adv. Funct. Mater.* **2020**, *30* (52), 2006883.
16. Jian, T.; Zhou, Y.; Wang, P.; Yang, W.; Mu, P.; Zhang, X.; Zhang, X.; Chen, C.-L., Highly stable and tunable peptoid/hemin enzymatic mimetics with natural peroxidase-like activities. *Nature Commun.* **2022**, *13* (1), 3025.
17. Wang, S.; Yue, L.; Li, Z.-Y.; Zhang, J.; Tian, H.; Willner, I., Light-Induced Reversible Reconfiguration of DNA-Based Constitutional Dynamic Networks: Application to Switchable Catalysis. *Angew. Chem. Int. Ed.* **2018**, *57* (27), 8105-8109.

18. Lin, L.; Pang, W.; Jiang, X.; Ding, S.; Wei, X.; Gu, B., Light amplified oxidative stress in tumor microenvironment by carbonized hemin nanoparticles for boosting photodynamic anticancer therapy. *Light: Sci. Appl.* **2022**, *11* (1), 47.
19. Zhang, S.; Sun, X.; Wang, Z.; Sun, J.; He, Z.; Sun, B.; Luo, C., Molecularly Self-Engineered Nanoamplifier for Boosting Photodynamic Therapy via Cascade Oxygen Elevation and Lipid ROS Accumulation. *ACS Appl. Mater. Interfaces* **2022**, *14* (34), 38497-38505.
20. Yang, B.; Lu, Y.; Jiang, D.; Li, Z.; Zeng, Y.; Zhang, S.; Ye, Y.; Liu, Z.; Ou, Q.; Wang, Y.; Dai, S.; Yi, Y.; Huang, J., Bioinspired Multifunctional Organic Transistors Based on Natural Chlorophyll/Organic Semiconductors. *Adv. Mater.* **2020**, *32* (28), 2001227.
21. Tran, H.; Nikzad, S.; Chiong, J. A.; Schuster, N. J.; Peña-Alcántara, A. E.; Feig, V. R.; Zheng, Y.-Q.; Bao, Z., Modular Synthesis of Fully Degradable Imine-Based Semiconducting p-Type and n-Type Polymers. *Chem. Mater.* **2021**, *33* (18), 7465-7474.
22. Chen, C.-K.; Lin, Y.-C.; Ho, J.-C.; Yang, W.-C.; Chen, W.-C., Biomass-Derived Degradable Poly(azomethine)s for Flexible Bistable Photonic Transistor Memories. *ACS Sustainable Chem. Eng.* **2022**, *10* (16), 5268-5277.
23. Tran, H.; Feig, V. R.; Liu, K.; Wu, H.-C.; Chen, R.; Xu, J.; Deisseroth, K.; Bao, Z., Stretchable and Fully Degradable Semiconductors for Transient Electronics. *ACS Cent. Sci.* **2019**, *5* (11), 1884-1891.
24. Shi, C.; Zou, Z.; Lei, Z.; Zhu, P.; Zhang, W.; Xiao, J., Heterogeneous integration of rigid, soft, and liquid materials for self-healable, recyclable, and reconfigurable wearable electronics. *Sci. Adv.* **2020**, *6* (45), eabd0202.
25. Zhao, S.; Abu-Omar, M. M., Recyclable and Malleable Epoxy Thermoset Bearing Aromatic Imine Bonds. *Macromolecules* **2018**, *51* (23), 9816-9824.
26. Wang, Z.; Zhang, J.; Xing, R.; Yuan, J.; Yan, D.; Han, Y., Micropatterning of Organic Semiconductor Microcrystalline Materials and OFET Fabrication by "Hot Lift Off". *J. Am. Chem. Soc.* **2003**, *125* (50), 15278-15279.
27. Su, Y.; Wang, C.; Xie, W.; Xie, F.; Chen, J.; Zhao, N.; Xu, J., Low-Voltage Organic Field-Effect Transistors (OFETs) with Solution-Processed Metal-Oxide as Gate Dielectric. *ACS Appl. Mater. Interfaces* **2011**, *3* (12), 4662-4667.
28. Uchida, H.; Reddy, P. Y.; Nakamura, S.; Toru, T., Novel Efficient Preparative Method for Phthalocyanines from Phthalimides and Phthalic Anhydride with HMDS. *J. Org. Chem.* **2003**, *68* (22), 8736-8738.
29. Shaabani, A.; Maleki-Moghaddam, R.; Maleki, A.; Rezayan, A. H., Microwave assisted synthesis of metal-free phthalocyanine and metallophthalocyanines. *Dyes Pigm.* **2007**, *74* (2), 279-282.
30. Sharma, U.; Kumar, P.; Kumar, N.; Kumar, V.; Singh, B., Highly Chemo- and Regioselective Reduction of Aromatic Nitro Compounds Catalyzed by Recyclable Copper(II) as well as Cobalt(II) Phthalocyanines. *Adv. Synth. Cat.* **2010**, *352* (11-12), 1834-1840.

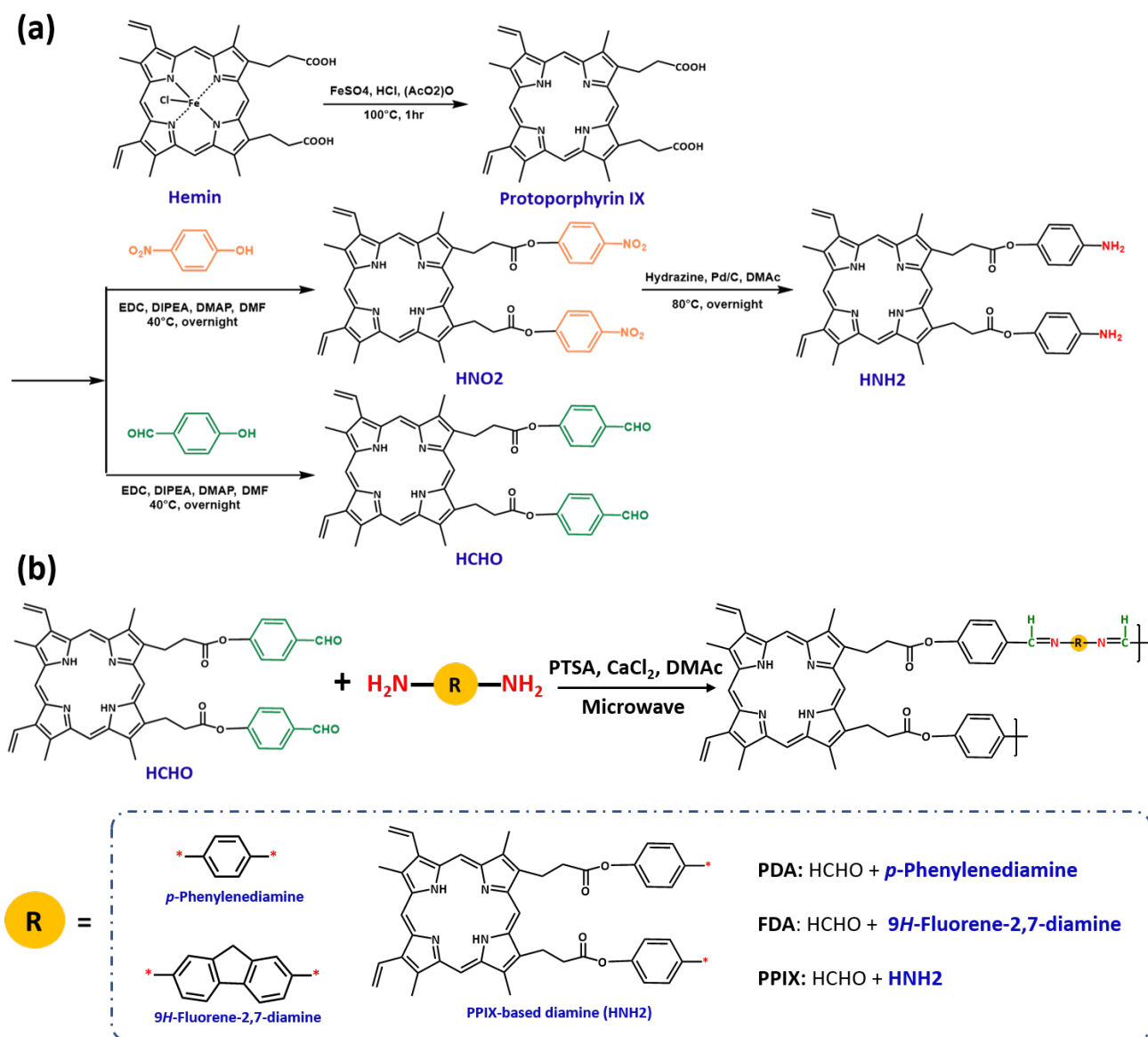
31. Ding, X.; Wei, S.; Bian, H.; Zhu, L.; Xia, D., Insights into the Self-Aggregation of Porphyrins and Their Influence on Asphaltene Aggregation. *Energy Fuels* **2021**, *35* (15), 11848-11857.
32. Stradomska, A.; Knoester, J., Shape of the Q band in the absorption spectra of porphyrin nanotubes: Vibronic coupling or exciton effects? *J. Chem. Phys.* **2010**, *133* (9), 094701.
33. Melville, O. A.; Lessard, B. H.; Bender, T. P., Phthalocyanine-Based Organic Thin-Film Transistors: A Review of Recent Advances. *ACS Appl. Mater. Interfaces* **2015**, *7* (24), 13105-13118.
34. Chen, C.-H.; Wang, Y.; Tatsumi, H.; Michinobu, T.; Chang, S.-W.; Chiu, Y.-C.; Liou, G.-S., Novel Photoinduced Recovery of OFET Memories Based on Ambipolar Polymer Electret for Photorecorder Application. *Adv. Funct. Materials* **2019**, *29* (40), 1902991.
35. Lin, Y.-C.; Yang, W.-C.; Chiang, Y.-C.; Chen, W.-C. Recent Advances in Organic Phototransistors: Nonvolatile Memory, Artificial Synapses, and Photodetectors. *Small Sci.* **2022**, *2*, 2100109.

TABLE AND FIGURES

Table 1. Molecular weight information, thermal/optical properties, energy levels, and memory device parameters of the biobased polyazomethines studied.

	Biomass content (%)^a	M_n^b	M_w^b	D^b	T_g (°C) ^c	E_g^{opt} (eV) ^d	HOMO (eV) ^e	LUMO (eV) ^f	ΔV_{th} (V) ^g	I_{on}/I_{off}^h
PDA	70.1	8,100	22,400	2.77	--	2.71	-4.73	-2.02	12.0	3.2×10^2
FDA	60.2	7,500	32,200	4.30	30	2.70	-5.05	-2.35	31.4	1.9×10^3
PPIX	79.6	10,000	36,800	3.68	60	2.73	-4.69	-1.96	38.7	1.0×10^2

^a Percentage of hemin-derivatives, protoporphyrin, divided by total weight based on a repeating unit of the polyazomethine. ^b Extracted from the SEC with UV light (280 nm) sources (solvent: DMF, relative to polystyrene standards). ^c Obtained from the second heating profiles with the ramping rate of 10 °C min⁻¹. ^d Obtained from the absorption onset wavelength (λ_{onset}) of the UV-vis absorption according to the formula: E_g^{opt} (eV) = 1240/ λ_{onset} . ^e HOMO energy levels estimated from the onset oxidation potentials (E_{onset}^{ox}) with CV on the basis of the reference energy level of ferrocene (-4.8 eV). The corresponding equation was HOMO = - eV (E_{onset}^{ox} - $E_{1/2}$ (ferrocene) + 4.8), where $E_{1/2}$ (ferrocene) is 0.106 eV. ^f The resulting LUMO was determined from the equation: LUMO (eV) = HOMO + E_g^{opt} . ^g Memory window determined from the contrast of the ON/OFF threshold voltages. ^h Memory ratio obtained from the ON/OFF currents ratio at $V_g = -20$ V.



Scheme 1. Synthetic routes for the (a) hemin-based monomers and (b) biobased polyazomethines.

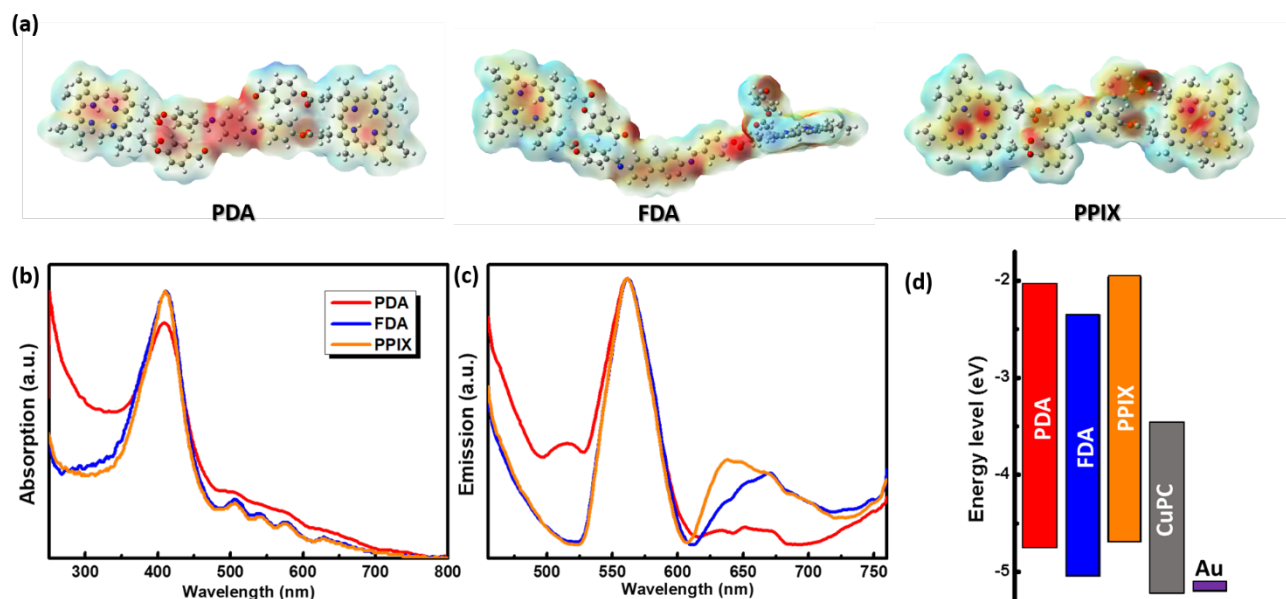


Figure 1. (a) ESP mapping of **PDA** (left), **FDA** (middle), and **PPIX** (right) derived from the optimized molecular geometries in DFT calculations with the method of B3LYP and a basis set of 6-31G. (b) UV-vis absorption and (c) PL emission spectra of **PDA**, **FDA**, and **PPIX** in the film state with a solvent of DMF. Note that the excitation wavelength in the photoluminescence emission spectra is 400 nm. (d) Energy level diagram of CuPC and biobased polyazomethines.

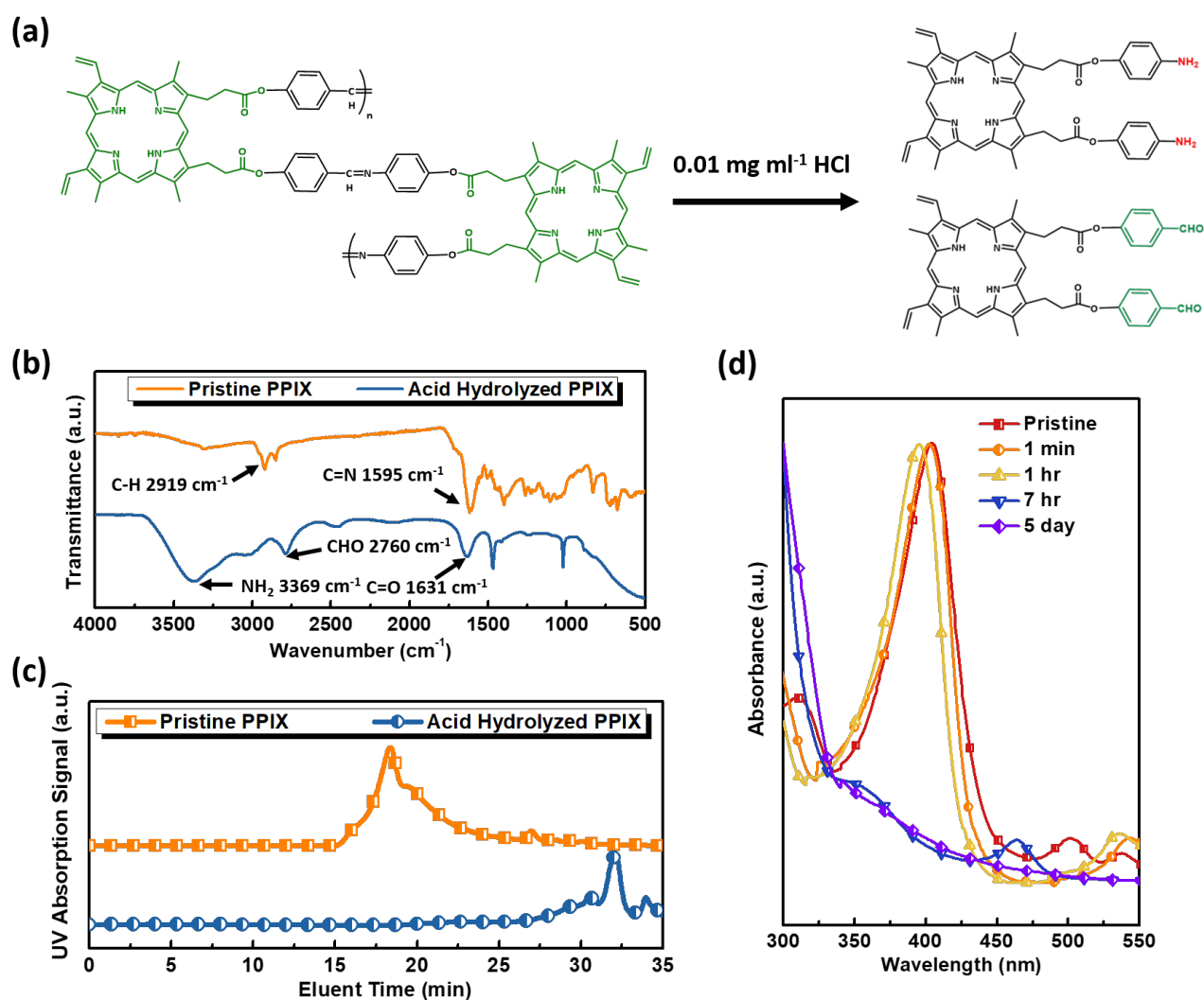


Figure 2. (a) Reaction scheme of the acid-hydrolyzing PPIX. Degradation studies of PPIX treated with 0.01 M HCl in DMF: (b) UV-vis absorption spectra of the acid hydrolyzed PPIX after different treating durations spanning the range of 1 min to 5 days; (c) FT-IR spectra, and (d) SEC profile detected by using 280-nm UV light.

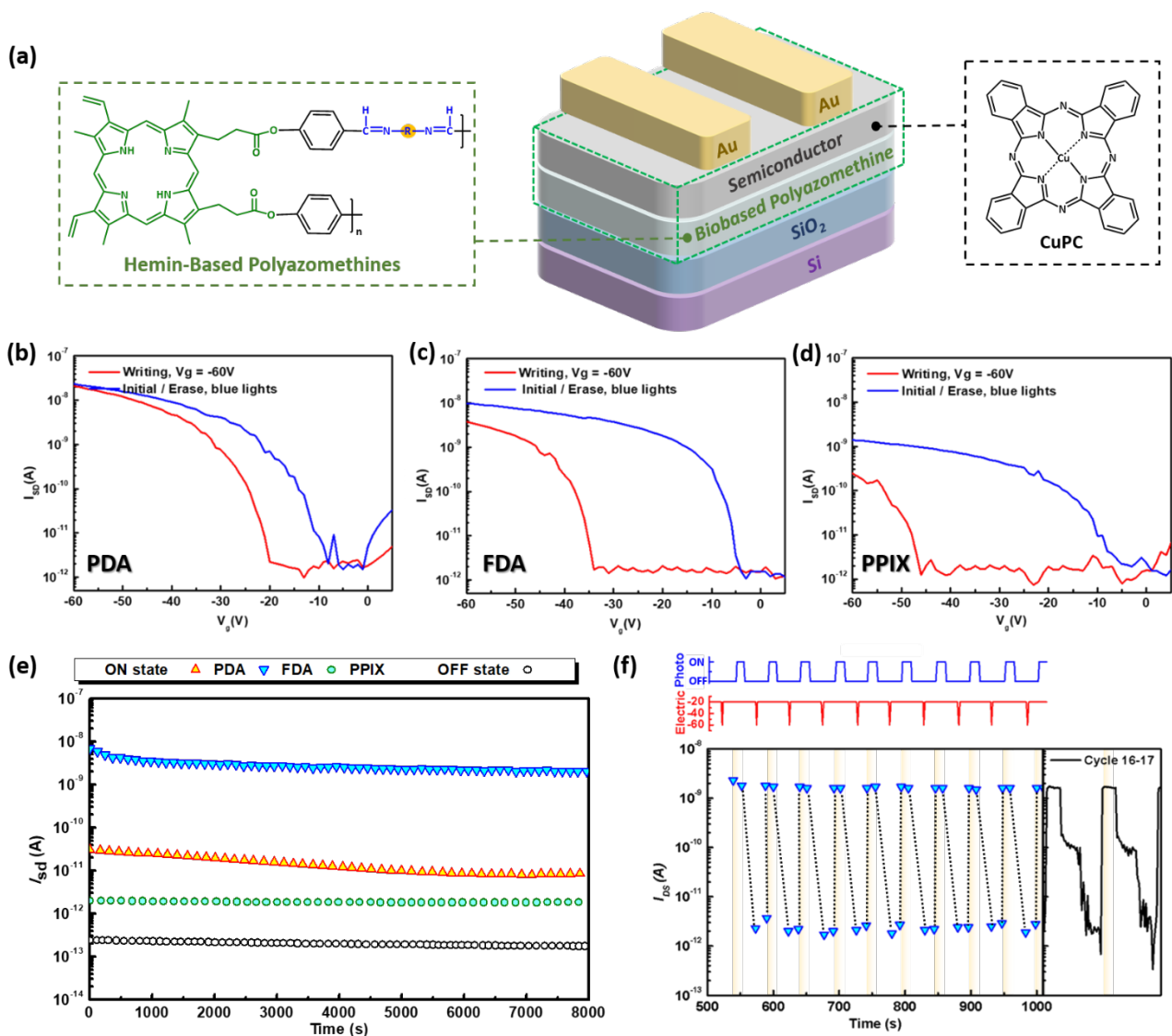


Figure 3. (a) Device architecture of the phototransistor memory and the chemical structures of constituent materials including CuPC and biobased polyazomethines. Transfer curves of the fabricated phototransistor memory comprising (b) **PDA**, (c) **FDA**, and (d) **PPIX**, at $V_d = -60$ V with electrical writing of $V_g = -60$ V and blue-light programming at $V_d = -60$ V. Note that the photoprogramming was performed under blue light (450 nm; 0.95 mW cm⁻²; 5 s) illumination. (e) Measurements of long-term stability test at $V_d = -60$ V and $V_g = -20$ V over 8000 s with electrical writing of $V_g = -60$ V for 1 s to achieve the low-current state and photoerasing (450 nm; 0.95 mW cm⁻²; 1 s) to achieve the high-current state. (f) Cyclic measurements of memory endurance test of the **FDA**-based device. The yellow-shaded area indicates the duration of 450-nm light illumination (intensity: 0.95 mW cm⁻²; $V_d = -20$ V; 10 s). The electrical writing was conducted by applying $V_g = -60$ V for 1 s; and the reading was conducted at $V_d = -20$ V.

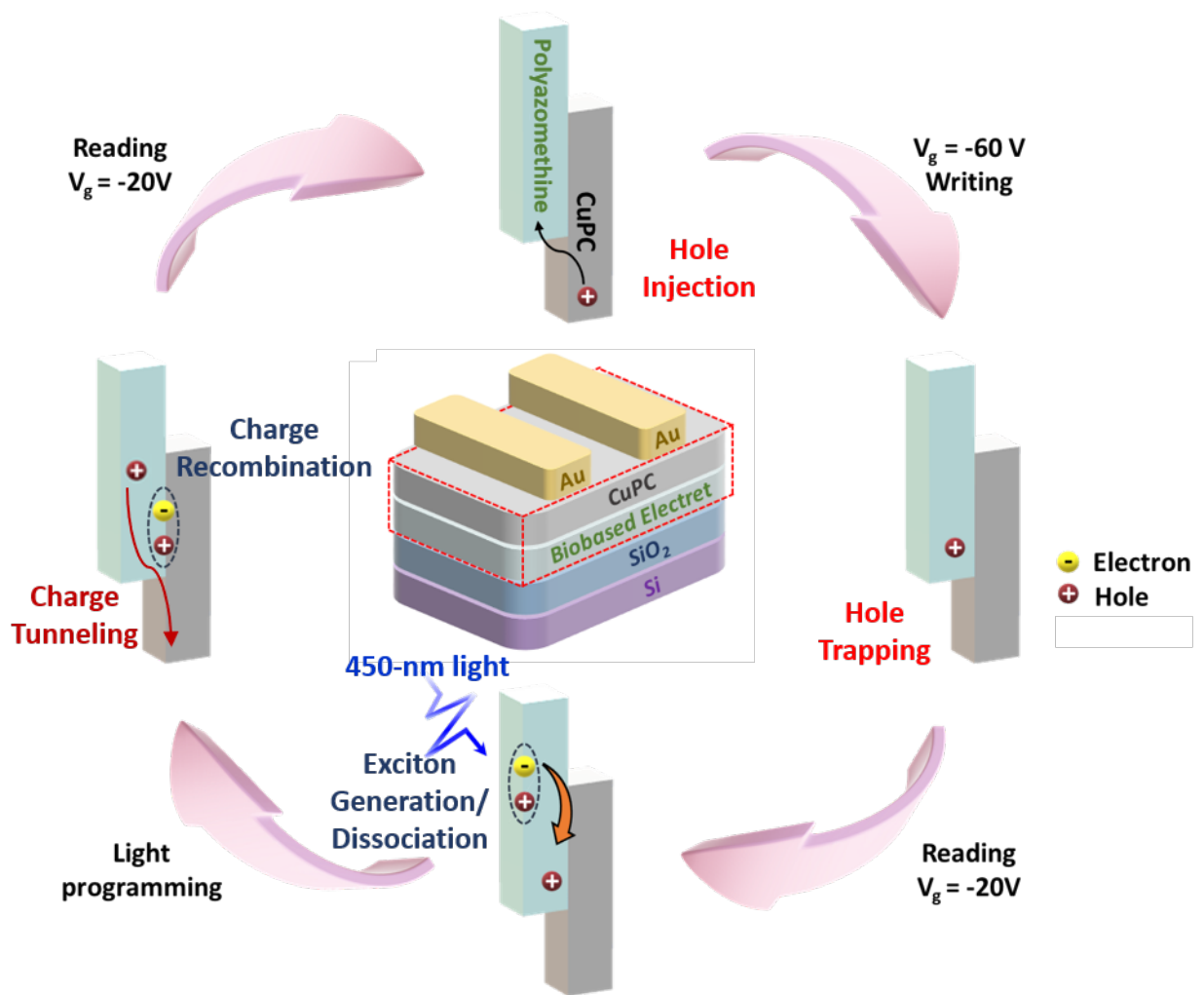


Figure 4. Visualization of the operating mechanism for the photoinduced recovery in the phototransistor memory comprising biobased polyazomethines.

TABLE OF CONTENTS FIGURE

